Fluid Dynamics and Co-located Conferences
June 24-27, 2013, San Diego, CA
21st AIAA Computational Fluid Dynamics Conference

RANS-based Aerodynamic Shape Optimization of a Blended-Wing-Body Aircraft

Zhoujie Lyu*
Joaquim R. R. A. Martins†
Department of Aerospace Engineering, University of Michigan, Ann Arbor, MI

A series of RANS-based aerodynamic shape optimization for an 800-passenger blended-wing-body aircraft is performed. A gradient-based optimization algorithm and a parallel structured multiblock RANS solver with Spalart–Allmaras turbulence model are used. The derivatives are computed using a discrete adjoint method considering both frozen-turbulence and full-turbulence assumptions. A total of 274 shape and planform design variables are considered. The objective function is the drag coefficient at nominal cruise condition. Lift, trim and root bending moment are constrained. Control surfaces at the rear centerbody are used to trim the aircraft via a nested free-form deformation volume approach. The optimized design is trimmed and stable in both on- and off-design conditions. The drag coefficient of the optimized design is reduced by 37 counts with trim and bending moment constraints satisfied. The addition of planform design variables provide an additional 2 drag count reduction.

I. Introduction

Fuel burn has become the largest contributor to the direct operating cost of airlines due to the increasing price of fuel. The fuel cost per passenger-mile has more than doubled from 2001 to 2010 [1]. For this reason, current research in aircraft design is placing more emphasis on fuel burn reduction than ever before. One of the most promising studies to reduce fuel burn is the design of unconventional aircraft configurations. Unconventional aircraft configurations, such as the blended-wing-body (BWB) configuration, have the potential to significantly reduce emissions and noise of future aircraft.

The BWB configuration is characterized by an airfoil-shaped centerbody that integrates payload, propulsion, and control surfaces. Compared to the classic wing-and-tube fuselage configuration, the BWB has superior aerodynamic performance [2, 3, 4]: the reduction in wetted area substantially reduces skin friction drag; the all-lifting design reduces wing loading and improves the spanwise lift distribution; the smooth blended wing-centerbody intersection reduces interference drag; and the area-ruled shape of the BWB reduces wave drag at high transonic speeds. The centerbody provides a substantial portion of total lift, thus reducing the wing-loading and resulting in a higher overall L/D. The low wing-loading allows the BWB to have excellent low-speed flight characteristics as well, making heavy high lift mechanisms, such as double-slotted flaps, redundant. The cross-sectional area of the BWB is similar to the Sears–Haack body, which results in lower wave drag at transonic speeds, according to Whitcomb's area rule [5]. Despite various aerodynamic benefits, the aerodynamic shape of the BWB also brings challenges to the design process. The complex shape of the BWB may cause difficulty during manufacturing. Without the conventional empennage, the chordwise lift distribution on the centerbody needs to be carefully designed to maintain a positive static margin. The thick airfoil shape of the centerbody also makes it a challenge for the BWB to achieve low drag and generate sufficient lift at a reasonable deck angle.

Several authors have previously investigated the aerodynamic shape optimization of the BWB configuration. Liebeck [6, 2] and Wakayama [7, 8] presented the multidisciplinary design optimization (MDO) of the Boeing BWB-450 using a vortex-lattice aerodynamic solver. The trim and stability of the BWB have also been considered. Qin *et al.* [4, 9] performed a progressive aerodynamic optimization of the European MOB BWB geometry, including inverse design and 3D shape optimization with a trim constraint. Peigin and Epstein [10] used a genetic algorithm and

*PhD Candidate, Department of Aerospace Engineering, University of Michigan, AIAA Student Member
†Associate Professor, Department of Aerospace Engineering, University of Michigan, AIAA Associate Fellow

reduced-order methods to perform a multipoint drag minimization of the BWB.

Kuntawala *et al.* [11, 12] studied BWB planform and shape drag minimization using a Euler adjoint implementation. Meheut *et al.* [13] performed a shape optimization of the AVECA flying wing planform subject to a low-speed takeoff rotational constraint. A frozen-turbulence RANS adjoint was used to compute the gradient in that case. Lyu and Martins [14] investigated the Euler-based BWB shape optimization with bending moment, trim, and static margin constraints. The work presented in this paper extends the previous studies to RANS-based aerodynamic shape optimization. An efficient automatic differentiated adjoint of the Navier–Stokes equations with a Spalart–Allmaras turbulence model is used [15]. We performed a series of aerodynamic shape and planform optimization studies. Trim and stability conditions of the BWB at both low-speed and high-speed are examined. The BWB aircraft is trimmed at multiple flow conditions using nested free-form-deformation (FFD) to simulate the effect of the control surfaces. Finally, the effects of the frozen-turbulence assumption on the numerical accuracy and optimization convergence are assessed.

The paper is organized as follows. The numerical tools used in this work are summarized in Section II. The problem formulation, mesh, and the baseline geometry are discussed in Section III. Finally, results from the aerodynamic shape optimization are presented in Section IV.

II. Methodology

This section describes the numerical tools used in the aerodynamic shape optimization of the BWB aircraft. These tools are components of the MDO for aircraft configurations with high fidelity (MACH) [16, 17].

A. Geometric Parametrization

A free-form-deformation (FFD) approach is used to parametrize the geometry [18]. The FFD volume parametrizes the geometry changes rather than the geometry itself, resulting in a more efficient and compact set of geometry design variables, making it easier to handle complex geometrical manipulations. Any geometry may be embedded inside the volume by performing a Newton search to map the parameter space to physical space. All the geometric changes are performed on the outer bound box, the FFD volume. Any modification on the FFD volume can be used to indirectly modify the embedded objects.The key assumption of the FFD approach is that the geometry has constant topology throughout the optimization process, which is often the case for wing design. In addition, since FFD volumes are trivariate B-spline volumes, the sensitivity information of any point inside the volume can be easily computed. Figure 1 shows the FFD volume and geometric control points for the BWB aerodynamic shape optimization.

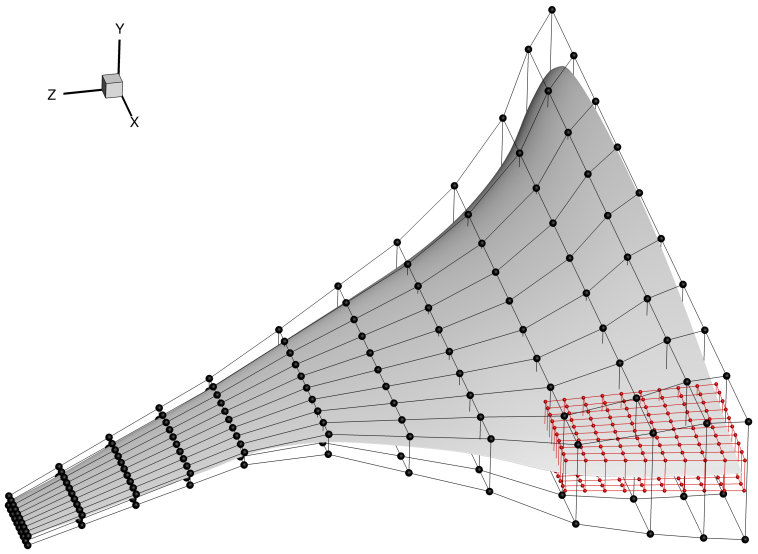

Figure 1. FFD volume (black), and control surface sub-FFD volume (red) with their respective control points

The BWB uses control surfaces on its rear centerbody, which are analogous to elevators on conventional configuration, to trim the aircraft. To simulate these control surfaces, a nested FFD volume approach is used as shown in Figure 1. The sub-FFD is embedded in the main FFD, similar to the embedding of the aircraft geometry itself. Any changes in the main FFD can be propagated to the sub-FFD. The sub-FFD is set to rotate about the hinge line of the control surface. Once the sub-FFD rotates, the embedded geometry changes the local shape accordingly. Due to the constant topology assumption of the FFD approach, and the limitation of mesh warping, the surface has to be continuous around the control surfaces, eliminating the elevator gap. Therefore, when control surfaces deflect, there is a transition region between the control surface and the centerbody, similar to those studied in a continuous morphing wing [19]. Figure 2 shows the sub-FFD volume and the geometry at a 25 degree trim angle.

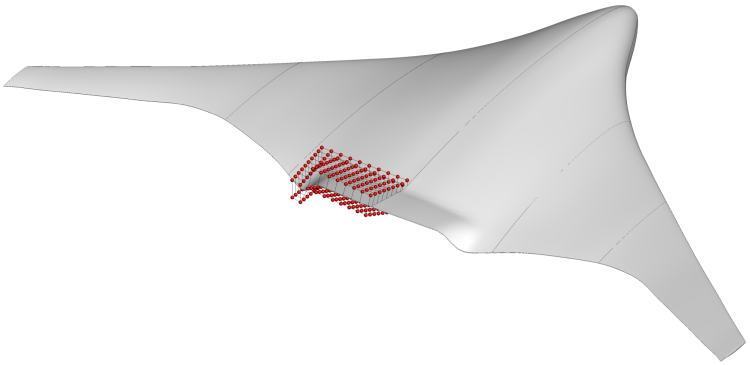

Figure 2. Sub-FFD volume and control points at 25 degree trim angle

In addition, the center-of-gravity (CG) locations of the centerbody and the outer wing sections are embedded in the main FFD. Any changes in planform shift the CG locations as well. The overall CG is then calculated based on the CG for each component. CG locations of the outer wing sections are positioned at 40% MAC of each section. CG locations of the centerbody is assumed to be positioned at 60% of the total length.

B. Mesh Perturbation

While FFD volumes handle modifications of the geometry, the mesh for CFD analysis needs to be altered to match the modified geometry. The mesh perturbation scheme used in this work is a hybridization of algebraic and linear elasticity methods [18]. The idea behind the hybrid warping scheme is to apply a linear elasticity-based warping scheme to a coarse approximation of the mesh to account for large, low-frequency perturbations, and to use the algebraic warping approach to attenuate small, high-frequency perturbations. The goal is to compute a similar, high quality perturbed mesh as obtained by using a linear elasticity scheme but at a much lower computational cost.

C. CFD Solver

The flow solver we use is the Stanford University multiblock (SUmb) [20] solver. SUmb is a finite-volume, cell-centered multiblock solver for the compressible Euler, laminar Navier–Stokes, and RANS equations (steady, unsteady, and time-periodic) and it provides options for a variety of turbulence models with one, two, or four equations, and options to use adaptive wall functions. The Jameson–Schmidt–Turkel (JST) scheme [21] augumented with artificial dissipation is used for the spatial discretization. The main flow is solved using an explicit multi-stage Runge–Kutta method along with a geometrical multi-grid scheme. The segregated Spalart–Allmaras (SA) turbulence equation is iterated with the diagonally dominant alternating direction implicit (DDADI) method. An automatic differentiation adjoint for the Euler and RANS equations was developed to compute the gradients [22, 15]. The adjoint implementation supports both the full-turbulence and frozen-turbulence modes. The adjoint equations are solved with preconditioned GMRES [23] using PETSc [24, 25, 26].

D. Optimization Algorithm

Due to the high computational cost of a CFD solver, it is critical to choose an efficient optimization algorithm that requires a reasonably low number of function calls. Gradient-free methods, such as genetic algorithms, have a higher probability of getting close to the global minimum for cases with multiple local minima. However, slow convergence and a large number of function calls would make gradient-free aerodynamic shape optimization infeasible with current computational resources, especially for large numbers of design variables. Therefore, we use a gradient-based optimizer combined with adjoint gradient evaluations to achieve an efficient optimization process. For a large number of design variables, the use of gradient-based optimizers is advantageous. We use a Python-based optimization package, pyOpt [27], to interface with the CFD and adjoint solvers. The underlying optimizer used in pyOpt is SNOPT (sparse nonlinear optimizer) [28], which is a gradient-based optimizer that implements a sequential quadratic programming (SQP) method. SNOPT is designed to solve large-scale nonlinear optimization problems with thousands of constraints and design variables. It uses a smooth augmented Lagrangian merit function and the Hessian of the Lagrangian is approximated using a limited-memory quasi-Newton method.

III. Problem Formulations

The BWB configuration has superior aerodynamics performance when compared to conventional configurations. In order to fully realize its potential, the external shape of the BWB has to be carefully designed. The primary focus of this study is drag minimization subject to a lift constraint. Additionally, the following constraints are considered: bending moment, trim, and static margin. In this section, we discuss the problem setup and the optimization formulation for the aerodynamic shape optimization of the BWB.

A. Baseline Geometry

The baseline geometry is shown in Figure 3. This is an 800-passenger BWB with a similar planform to the Boeing BWB-450-1L [2]. The baseline has a span of 276 ft and a total length of 144 ft. The geometry is divided into a centerbody section and an outer wing section. The CG of the centerbody is 83 ft from the nose, while the CG of the wing section is 125 ft from the nose. The overall CG is calculated based on the CG of each component, thus resulting in an overall CG location of 91 ft from the nose. Based on the baseline planform, the mean aerodynamic chord (MAC) is 86 ft. The baseline CG location corresponds to 55% MAC.

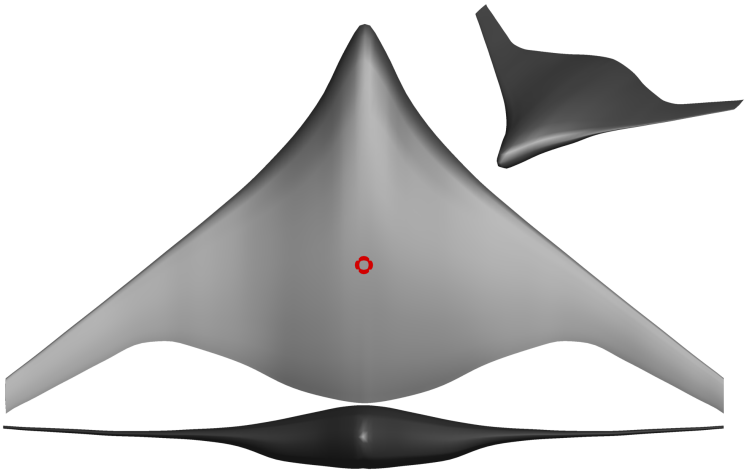

Figure 3. The baseline geometry of the BWB with CG location shown in red

The geometry is generated with a prescribed thickness-to-chord (t/c) ratio, as well as leading edge and trailing edge locations. We use the NASA SC(2)-0518 airfoil at the root and the NASA SC(2)-0410 airfoil at the tip. Table 1 summarizes the geometric parameters of the baseline BWB.

Geometry Parameters	Baseline BWB
Span	276 ft
Length	144 ft
Area	7760 ft^2
CG distance from the nose	91 ft
Mean aerodynamic chord	86 ft

Table 1. Geometric parameters for the baseline BWB

B. Grid Sensitivity

Mesh for the BWB is generated using an in-house hyperbolic mesh generator. The mesh is matched out from the surface mesh with a O-grid topology. The nominal cruise flow condition is at Mach 0.85 and 35,000 ft. Therefore, we use 100 million as the flight Reynolds number. The spacing on the first layer uses a y^+ of 0.5 to adequately resolve the boundary layer. The grid is matched out to a far field that is located at a distance of 25 spans, with an average growth ratio of 1.2. The grid that is used for the optimization has a size of 1.24 million cells. It is generated from a surface mesh of 17,700 cells. To determine the resolution accuracy of this grid, a grid convergence study is performed. All grids are generated using the hyperbolic mesh generator with a refined spacing. Figure 4 shows the drag polar of each mesh size. Figure 5 shows the mesh convergence plot.

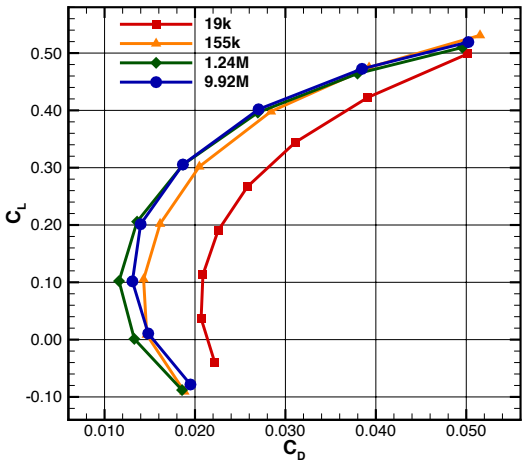

Figure 4. Drag polar of each BWB mesh size

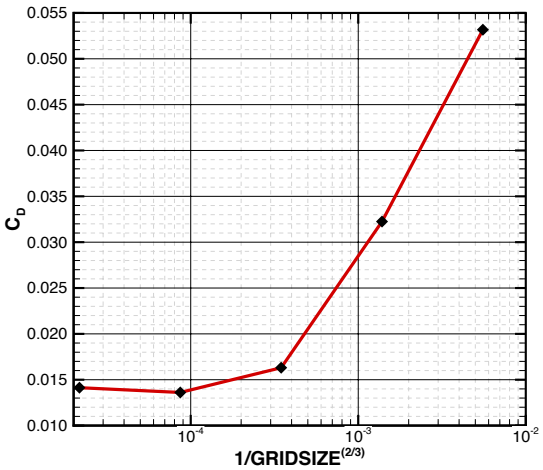

Figure 5. Mesh convergence plot of BWB grids at nominal cruise condition

As shown in the mesh convergence plot, the 1.24 million cell grid is within 5 drag counts of the 9.92 million cell grid result. We choose the 1.24 million grid size because it allows a reasonable optimization run time, while providing sufficient accuracy. The RANS flow solution can be obtained within 5 minutes from a cold start with 6 orders of residual reduction on 180 E5 processors. Figure 6 shows the BWB mesh on the surface and the symmetry plane. Figures 7 and 8 show the k-plane slice of the volume mesh at $k = 45$ and $k = 55$. The surface mesh near the transition region of elevator control surface is deliberately bunched to provide a smooth mesh transition and to maintain the mesh quality when the control surface is moved.

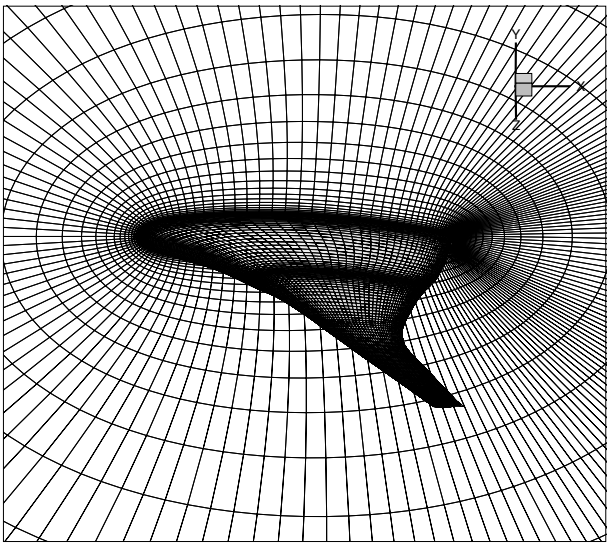

Figure 6. BWB mesh at the surface $k = 1$

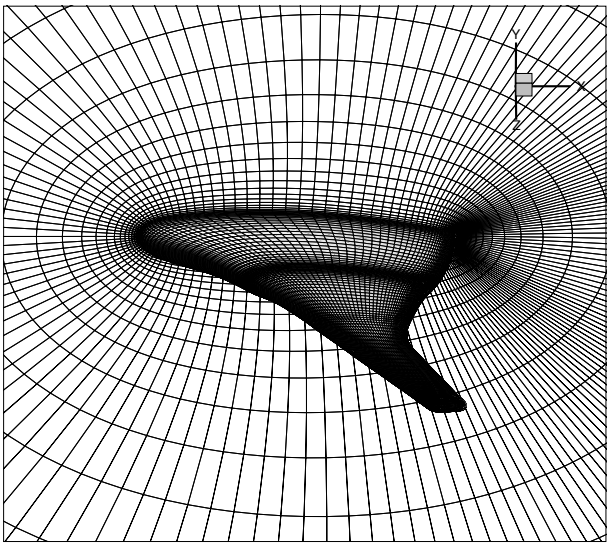

Figure 7. BWB mesh k-plane slice at $k = 45$

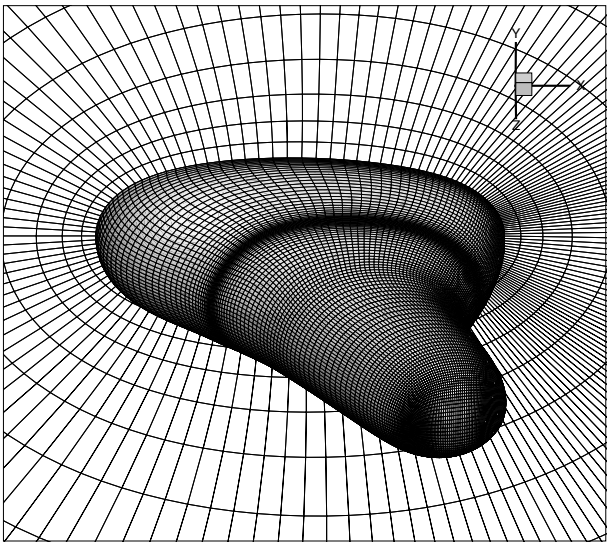

Figure 8. BWB mesh k-plane slice at $k = 55$

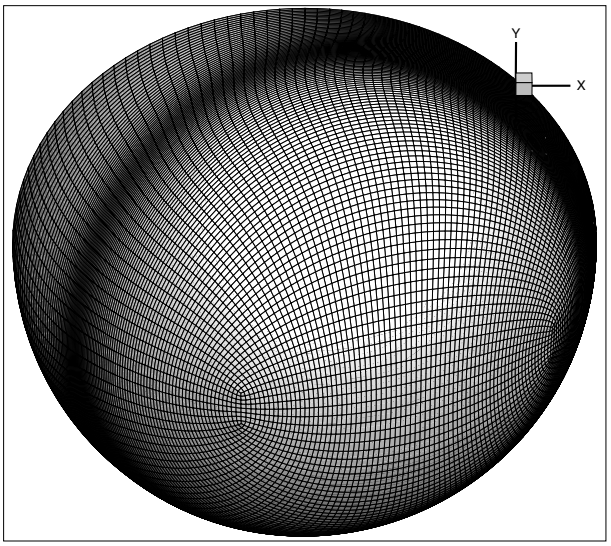

Figure 9. BWB mesh at the far field $k = 73$

C. Optimization Formulation

1. Objective Function

We choose drag coefficient at the nominal cruise condition as the objective function for the optimization subject to constrained lift coefficient. The drag coefficient consists of both pressure drag and viscous drag from the RANS solver. The lift coefficient is constrained to $C_L = 0.206$. Both lift and drag coefficients use planform area as the reference area, resulting in lower wing loading and lift coefficient.

2. *Design Variables*

The first set of design variables consists of the control points distributed on the FFD volume. A total of 240 shape variables are scattered on the lower and upper surfaces of the FFD volume, as shown in Figure 1. The large number of shape variables provides more degrees of freedom for the optimizer to explore, and to fine-tune the sectional airfoil shape and thickness-to-chord ratio at each spanwise location. Due to the efficient adjoint implementation, the cost of computing shape gradients is nearly independent of the number of shape variables [16].

The next set of design variables is the spanwise twist distribution. Ten section twist design variables are used. The center of twist rotation is fixed at the reference axis, which is located at the quarter chord of each section. The twist variables provide a direct control for the optimizer to minimize induced drag by adjusting the spanwise lift distribution, as well as to meet the root bending moment constraint.

Planform variables are also considered in the optimization, which can contribute to the reduction of wave drag. The sweep angle, chord length, and the width of the centerbody are kept constant. Only the planform variables of the outer wing are set as design variables. The outer wing is defined as the outer 60% of the total span, where wing-centerbody blending region ends. The outer wing is divided into seven sections. Each section has an independent set of planform variables, which are the sweep angle, chord length, and span of the section. Table 2 and Figure 10 summarize the design variable sets. By providing complete freedom of the outer wing, we allow the optimizer to better explore the optimal planform shape.

Design Variables	**Count**	**Design Variables**	**Count**
airfoil shape	240	angle-of-attack	1
twist	10	sweep	7
chord	7	span	7
Total	**274**		

Table 2. Summary of the design variables used in the BWB aerodynamic shape optimization problem

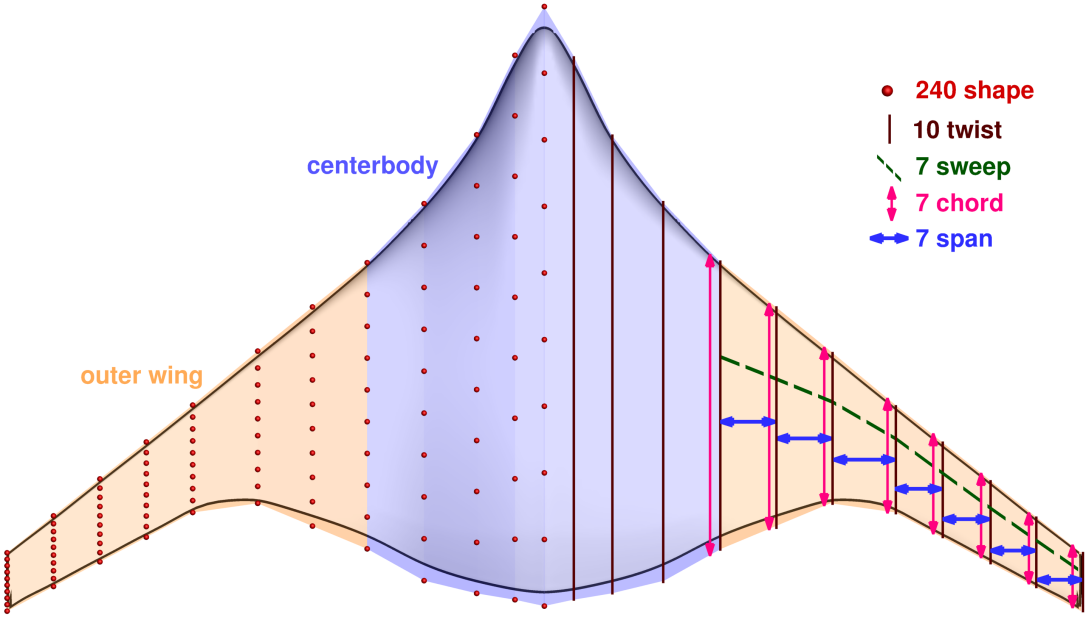

Figure 10. Illustration of the shape and planform design variables

3. Constraints

Since optimizers tend to explore any weaknesses in numerical models, an optimization problem needs to be carefully constrained in order to yield a physically feasible design. Several geometric constraints are implemented. First, we impose thickness constraints from 5% chord at the leading edge (LE) up to 95% chord near the trailing edge (TE). A total of 400 thickness constraints are imposed in the 20 by 20 grid. The constraints have a lower bound of 90% of the baseline thickness with no upper bound. These constraints ensure sufficient height in the centerbody cabin and sufficient thickness at the LE and TE for the installation of high-lift devices such as slats and flaps. The total volume of the centerbody and the wing is also constrained to meet requirements for the cabin and payload space as well as fuel volume. Finally, in order to avoid generating wavy LE and TE, shape variables located at the LE and TE are constrained so that each pair of shape variables on LE and TE can move only in opposite directions with equal magnitudes.

Due to the absence of a structural model, we use the bending moment at the center plane as a surrogate for the structural weight trade-offs. This bending moment is constrained to be less or equal to the baseline bending moment. The bending constraint is necessary to capture the trade-offs between aerodynamic performance and structural weight. However, it is possible to perform these trade-offs with more accuracy by using high-fidelity aerostructural optimization [17].

In addition, the BWB has to be trimmed at each flight condition. Ideally, the aircraft needs to be trimmed at nominal cruise condition without the need to deflect its control surfaces. Therefore, we freeze the sub-FFD, which rotates the trim control surface during the on-design optimization with the pitching moment constraint. The sub-FFD is then used in the analysis of off-design conditions.

In addition, stability is a particularly important design consideration of the BWB configuration. With the absence of a conventional empennage, it is not immediately obvious what is the best way to achieve a positive static margin for a BWB aircraft. The goal is to maintain positive static margin for all flight conditions. The static margin can be calculated as the ratio of the moment and lift derivatives [29]. We calculate C_{M_α} and C_{L_α} using finite difference with an angle-of-attack step size of 0.1 deg.

$$K_n = -\frac{C_{M_\alpha}}{C_{L_\alpha}}, \tag{1}$$

Table 3 summarizes the constraints for the optimization problems.

Constraints	**Count**	**Constraints**	**Count**
Lift coefficient	1	Trim	1
Thickness	400	LE, TE control points	40
Internal volume	1	**Total**	**443**

Table 3. Summary of the constraints used in the BWB aerodynamic shape optimization problems

IV. Results

A series of RANS-based BWB aerodynamic shape optimizations are performed. Gradients are computed with the adjoint method considering both full-turbulence and frozen-turbulence. A total of four cases are presented in this section.

Case 1: Baseline lift-constrained drag minimization with respect to shape variables, with geometric constraints
Case 2: Lift-constrained drag minimization with respect to shape variables, with geometric, bending moment, and trim constraints
Case 3: Lift-constrained drag minimization with respect to shape and planform variables, with geometric, bending moment, and trim constraints
Case 4: Lift-constrained drag minimization using full-turbulence adjoint

The computations are performed on high performance clusters with two six-core 2.67 GHz Intel Xeon X5650 processors per node. Each node has a total of 8 GB RAM. The cluster has InfiniBand networking for interconnections. The results and discussions for each case are presented in the following sections.

A. Case 1: Baseline lift-constrained drag minimization with respect to shape variables with geometric constraints

To validate our optimization formulation, we begin with a baseline optimization case with only geometric and lift constraints. The design variables are shape variables, twist, and angle-of-attack. Without any additional constraints, we expect to see a lift distribution that is close to elliptical and weakened shocks. Since only one flow solution and two adjoint systems need to be solved at each iteration, this problem requires less computational time than other cases. The optimization is performed using 180 cores, and converged in 8.3 hours after 37 major optimization iterations.

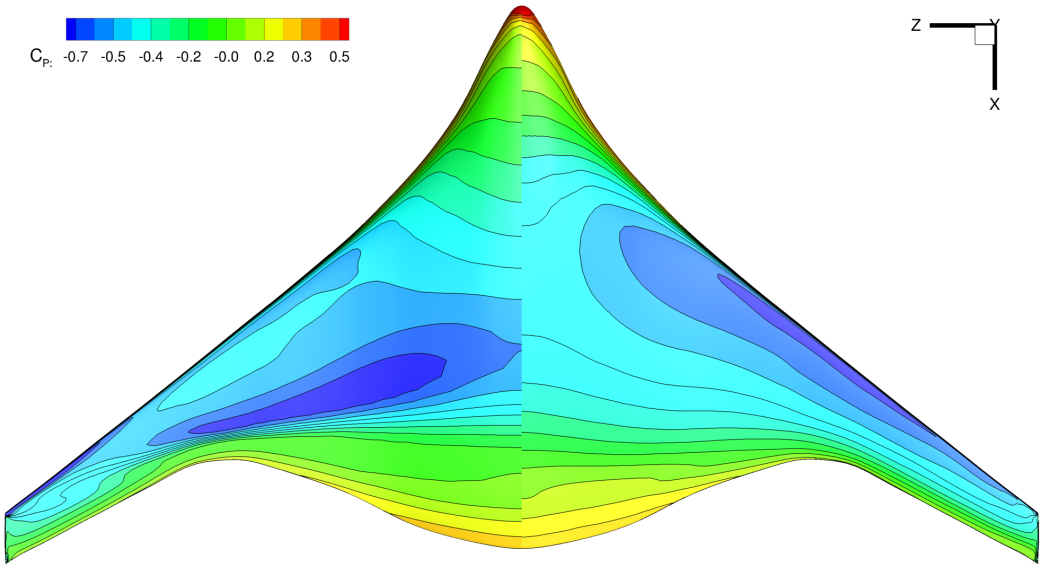

Figure 11. Pressure contour of the baseline and optimized BWB for Case 1

Figure 11 shows the pressure contour of the baseline and optimized BWB. The baseline BWB has clustered pressure contour lines near the wing kink at about 75% chord, which indicates the presence of a shock. The local pressure near the region increases rapidly, resulting in a higher wave drag. The optimized BWB shows parallel pressure contour lines with roughly equal spacing, indicating a shock-free solution. This is verified with the shock iso-surface plots shown in Figure 12. We can see that the baseline BWB has a strong shock on the upper surface, while the optimized design removed the shock completely at the design condition.

The shock elimination can also be seen on the section C_p distributions in Figure 13. z is the span direction and b is the span. At $z/b/2 = 0.6$ and $z/b/2 = 0.9$, the sharp increase in local pressure due to the shock becomes a gradual slope from the LE towards the TE. The magnitude of C_p is also lowered near the LE.

In addition to the wave drag, the lift-induced drag is also reduced by twisting the centerbody and wing. The resulting lift distribution is much closer to the optimal elliptical lift distribution, as shown in Figure 15. The points at the nominal cruise condition are shown in black. The lift is shifted outboard, while the sectional lift on the centerbody is significantly reduced. The majority of the shape changes is near the wing kink section near $z/b/2 = 0.6$, where the strong shock occurred on the baseline BWB. The twist angle at this section is increased to 4 degrees, and the t/c ratio is also increased slightly. Overall, pressure drag decreases from $C_{D_p} = 0.009558$ to $C_{D_p} = 0.005185$. Skin friction drag increases slightly for about 2 drag counts due to the change in t/c and twist. However, it is negligible compared to the reduction in pressure drag. Aerodynamic coefficients of the baseline and optimized BWB are listed in Table 4.

With the optimal lift distribution, lift is shifted towards the wing tip. We can see that the root bending moment increases by 19.5%, which indicates that a heavier structure would be required. Therefore, a center plane bending

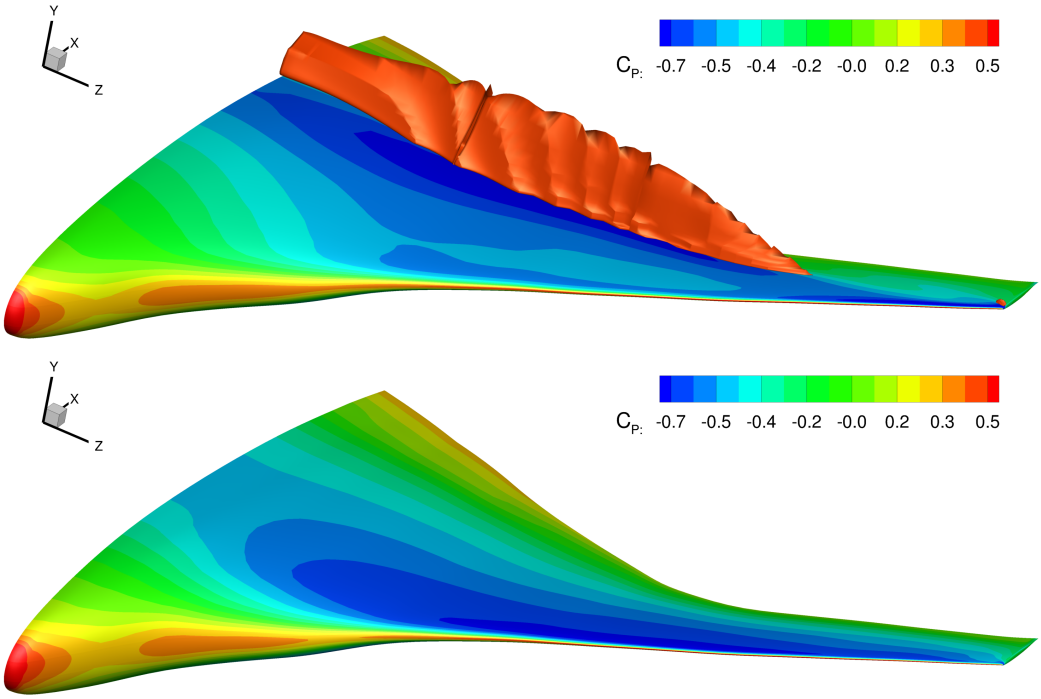

Figure 12. Shock surface on the baseline (top) and the optimized (bottom) BWB

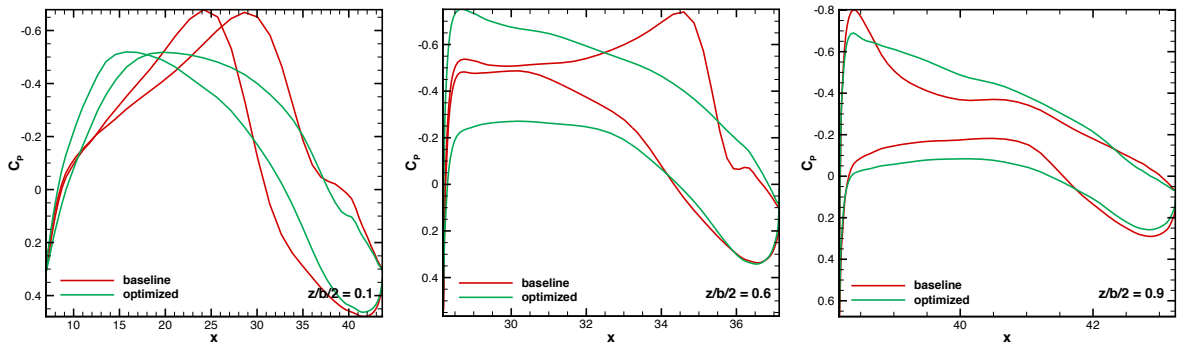

Figure 13. Sectional C_p distribution at $z/b/2 = 0.1$, $z/b/2 = 0.6$, and $z/b/2 = 0.9$

Coefficient	Baseline	Optimized	Difference
C_D	0.013609	0.009437	-30.7%
C_{D_P}	0.009558	0.005185	-45.8%
C_{D_V}	0.004050	0.004252	4.8%
C_M	0.05163	0.04525	-12.4%
C_{bend}	0.1195	0.1428	19.5%

Table 4. Aerodynamic coefficients of the baseline and optimized BWB in Case 1

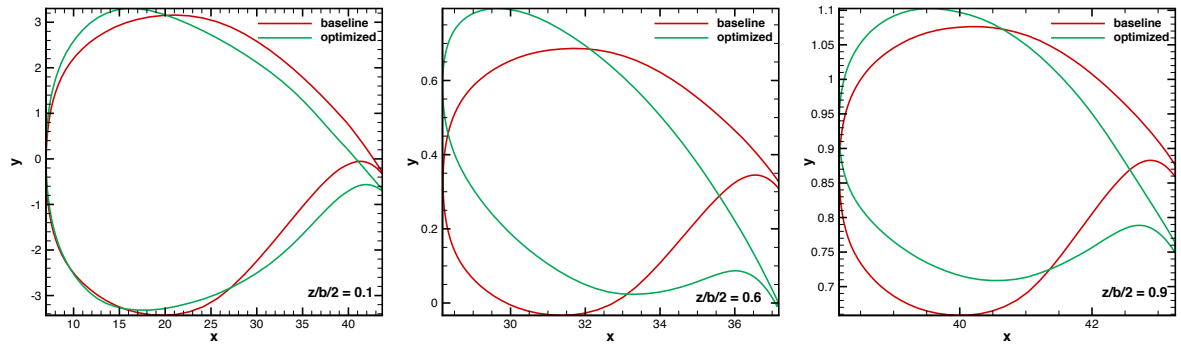

Figure 14. Sectional airfoil shape at $z/b/2 = 0.1$, $z/b/2 = 0.6$, and $z/b/2 = 0.9$

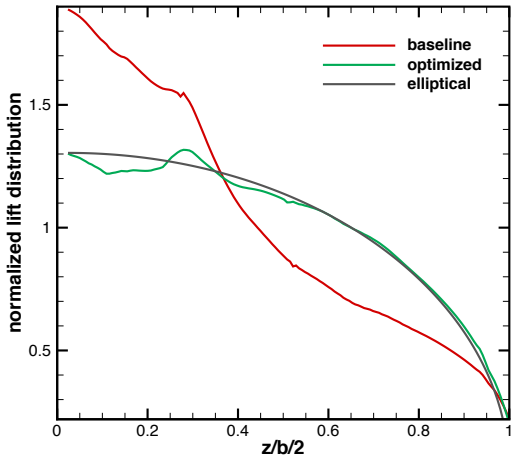

Figure 15. Baseline, optimized, and elliptical lift distribution for Case 1

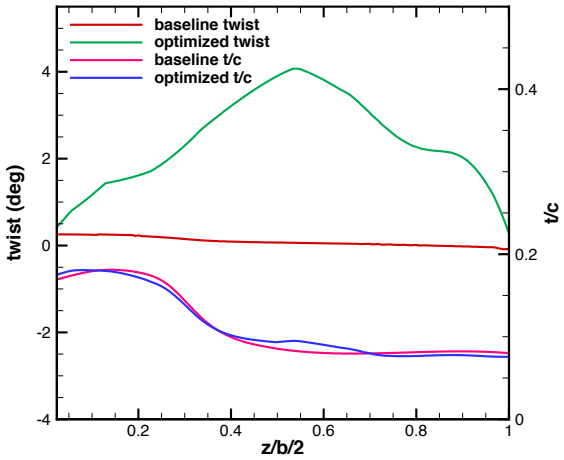

Figure 16. Twist and t/c distribution of the baseline and optimized BWB for Case 1

moment constraint is necessary to constrain the impact on structural weight. This baseline optimization serves as a validation of the optimization formulation. We obtain an elliptical lift distribution and reduced shock strength on the upper surface. We can also conclude that additional constraints are needed to achieve a practical design.

B. Case 2: lift-constrained drag minimization with respect to shape variables, with geometric, bending moment, and trim constraints

As discussed in the previous cases, we need to capture the trade-offs between aerodynamic performance, structural weight, and trim drag. For the BWB configuration, trim drag cannot be neglected during the optimization, since elevator trim would affect flow around the centerbody. Therefore, center plane bending moment and trim constraints are added. The bending moment is constrained to be less than or equal to the bending moment of the baseline configuration. Two additional adjoint systems are needed to compute the gradient of those constraints. This optimization problem converged in 14.5 hours using 180 cores, and required 45 optimization iterations.

Figure 17 shows the pressure contour of the baseline and optimized BWB. The pressure contour is very similar to Case 1, with slightly lower minimum C_p. The upper surface shock is also completely removed. The largest difference

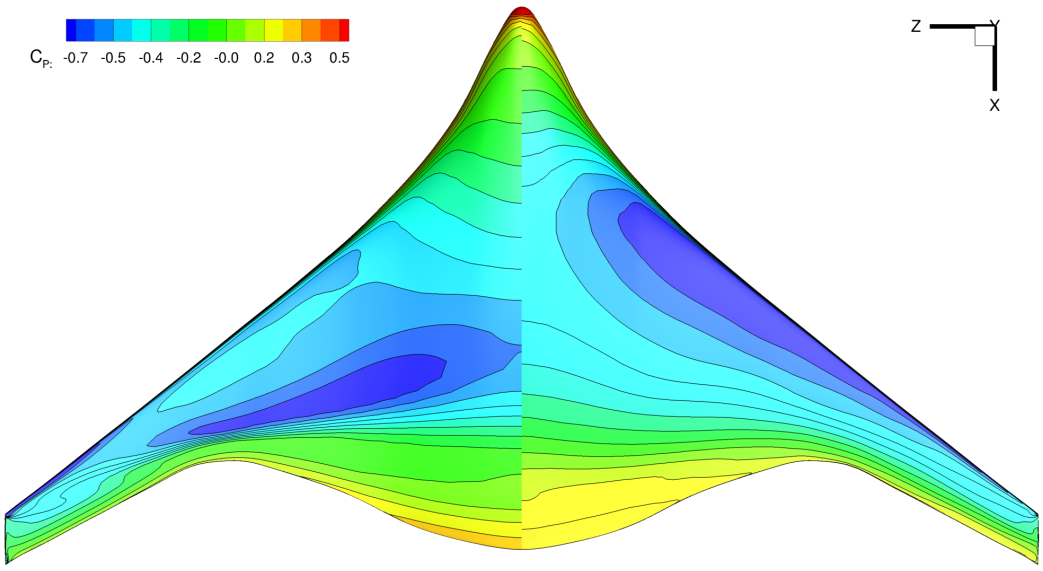

Figure 17. Pressure contour of the baseline and optimized BWB for Case 2

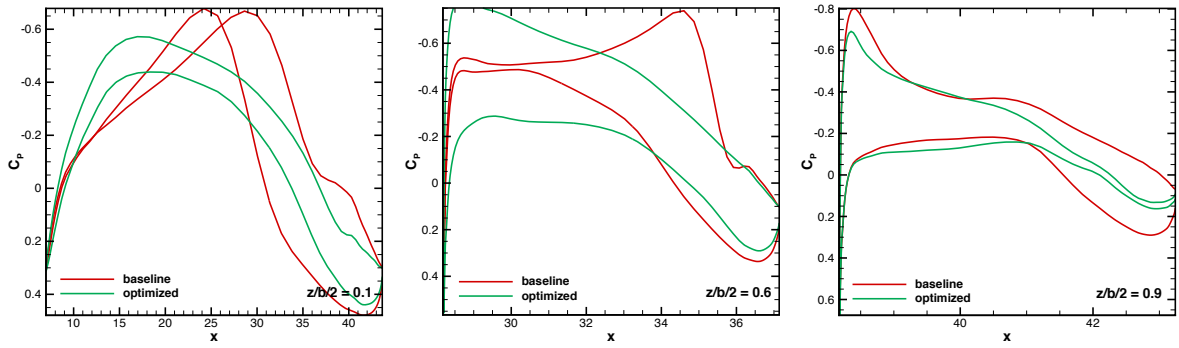

Figure 18. Sectional C_p distribution at $z/b/2 = 0.1$, $z/b/2 = 0.6$, and $z/b/2 = 0.9$ for Case 2

from Case 1 is near the wing tip. As shown in Figure 18, the wing tip $z/b/2 = 0.9$ is significantly unloaded compared to Case 1. The unloaded wing tip is driven by both bending moment and trim constraints.

The additional constraints also drive the lift and twist distributions. The centerbody still twists up, similarly to Case 1. However, the wing tip has a negative twist of 3 degrees. As a result, the optimized spanwise lift distribution is no longer elliptical. Lift on the wing section decreases linearly toward the wing tip. This departure from the elliptical lift distribution limits span efficiency and hinders improvements in induced drag. However, it benefits the structural weight and lateral control response for a flying wing. Two design features that lead to satisfaction of trim constraints on a trimmed flying wing are observed on the optimized BWB. The first is a reflex near the trailing edge of the airfoil at $z/b/2 = 0.9$, resulting in a significant change to the chordwise lift distribution at the tip. All lift is generated at the forward section of the wing, while the aft section has significantly less lift to trim the aircraft. Therefore, the net lift near the tip is reduced, as shown in Figure 20. The second feature is the unloaded wing tip. The optimized wing tip airfoil has washout and less lift than the baseline. The unloaded wing tips on a highly swept wing act as an horizontal tail to trim the aircraft.

Due to these constraints, the optimized drag coefficient is reduced by 37 counts as compared to 42 counts in the previous case. This change is primarily due to a lower span efficiency and the presence of the reflex centerbody airfoil,

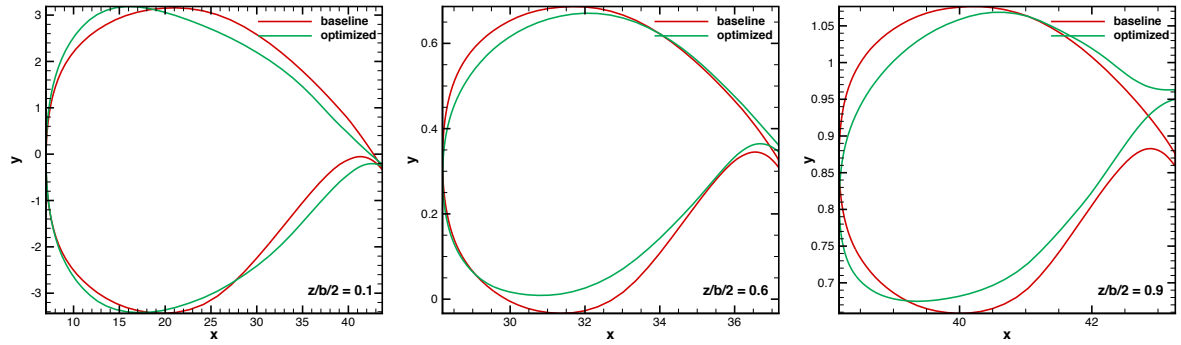

Figure 19. Sectional airfoil shape at $z/b/2 = 0.1$, $z/b/2 = 0.6$, and $z/b/2 = 0.9$ for Case 2

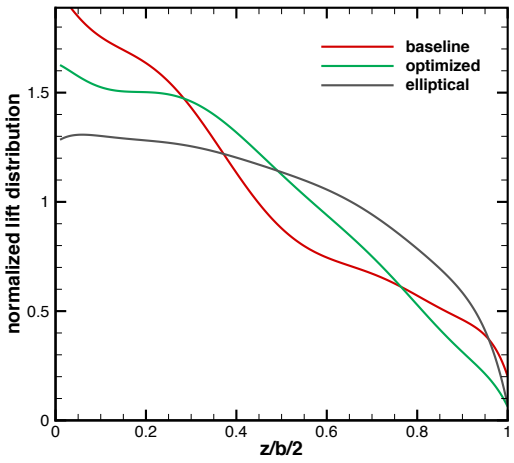

Figure 20. Baseline, optimized, and elliptical lift distribution

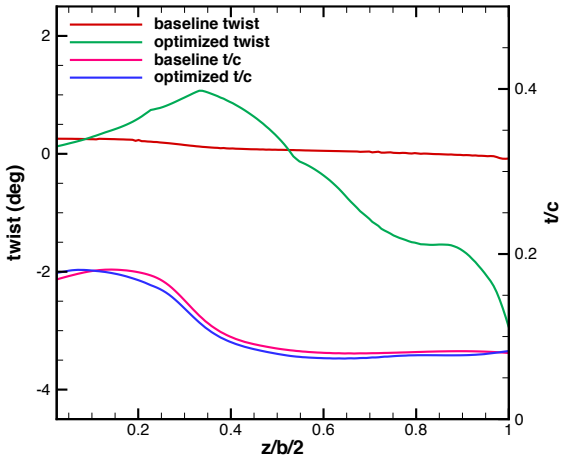

Figure 21. Twist and t/c distribution of the baseline and optimized BWB

which is less beneficial for the pressure drag. Aerodynamic coefficients of the baseline and optimized BWB are listed in Table 5.

Coefficient	Baseline	Optimized	Difference
C_D	0.013609	0.009885	-27.4%
C_{D_P}	0.009558	0.005652	-40.9%
C_{D_V}	0.004050	0.004233	4.5%
C_M	0.05163	0.0000	-100.0%
C_{bend}	0.1195	0.1195	0.0%

Table 5. Aerodynamic coefficients of the baseline and optimized BWB in Case 2

To investigate the off-design conditions, we perform a Mach sweep from 0.2 to 0.875. We use sub-FFD to deflect the control surface near rear centerbody to trim the aircraft at each condition. The results are compared with the baseline design in Figure 22. By comparing both trimmed baseline and optimized designs, we see that a trimmed

drag pocket is achieved in the transonic region from Mach 0.8 to 0.86. The baseline design starts the drag creep near Mach 0.8, while the optimized design significantly delays the drag creep. The drag coefficient of the optimized design remains nearly constant up to Mach 0.86.

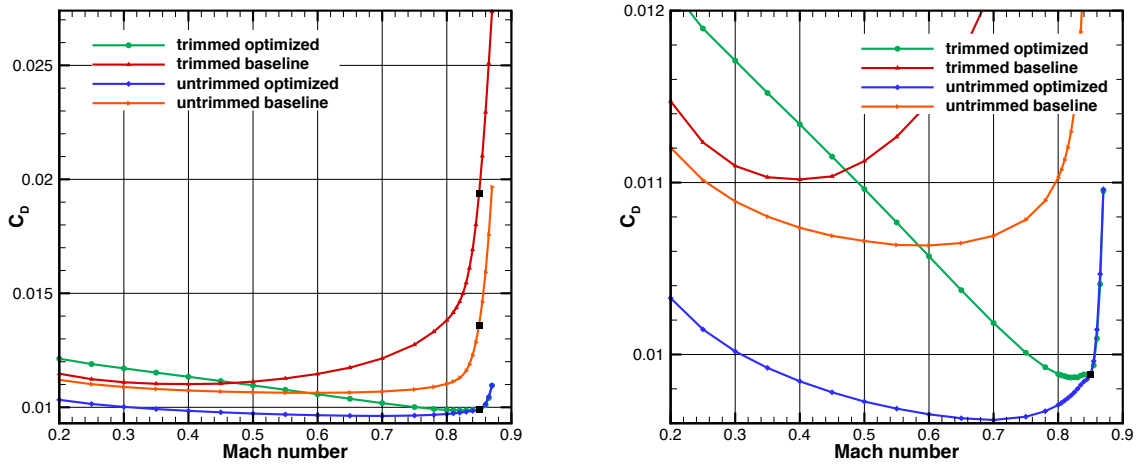

Figure 22. Mach divergence of the baseline and optimized BWB considering both trim and untrimmed conditions

In addition, by comparing the trimmed and untrimmed results, we can quantify the trim drag at each condition. We see that the baseline design has lower trim drag at low Mach numbers. Trim drag increases at high Mach numbers. The optimized design, however, trades the trim drag at low speeds for low trim drag at high Mach numbers. At low speeds, the optimized design has 18 counts of trim drag, while the trim drag is within 1 count near the nominal cruise condition. Figure 23 shows the trim drag of the baseline and optimized BWB.

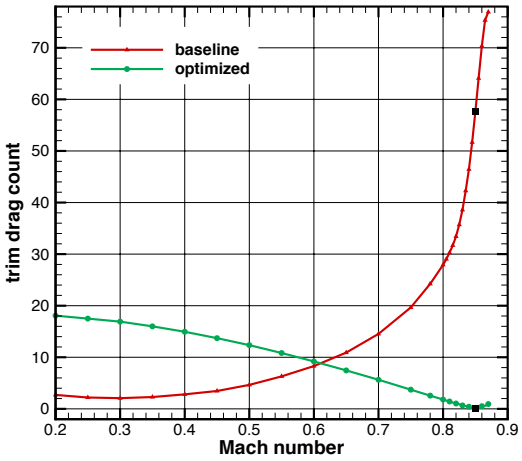

Figure 23. Trim drag of the baseline and optimized BWB

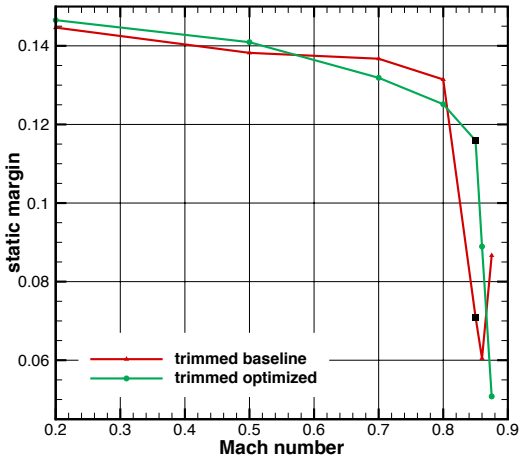

Figure 24. Static margin of the baseline and optimized BWB

The stability characteristics of the optimized design are also investigated. We compute the static margin at each Mach number using Equation (1). The center of pressure is nearly constant in the subsonic region. The static margin decreases slightly from 14% to 13% as Mach number increases from 0.2 to 0.8. In the transonic region beyond the nominal cruise condition, the static margin decreases rapidly from 13% to 5%. This is mostly because the flow is changes from a shock-free solution at Mach 0.85 to a flow with a strong shock at Mach 0.875, as shown in Figure 25.

The sectional C_p is dramatically different at high Mach numbers in the presence of shock, which results in a large change in C_{M_α} and C_{L_α}, as shown in Figure 26. Figure 27 shows the sectional C_p distribution at $z/b/2 = 0.6$ at Mach 0.85 and 0.875 with nominal angle-of-attack and perturbed angle-of-attack. We can see that C_{M_α} correlates well with the Mach divergence plot in Figure 22. C_{M_α} starts to change significantly near the drag creep Mach number, which is 0.8 for the baseline and 0.85 for the optimized BWB.

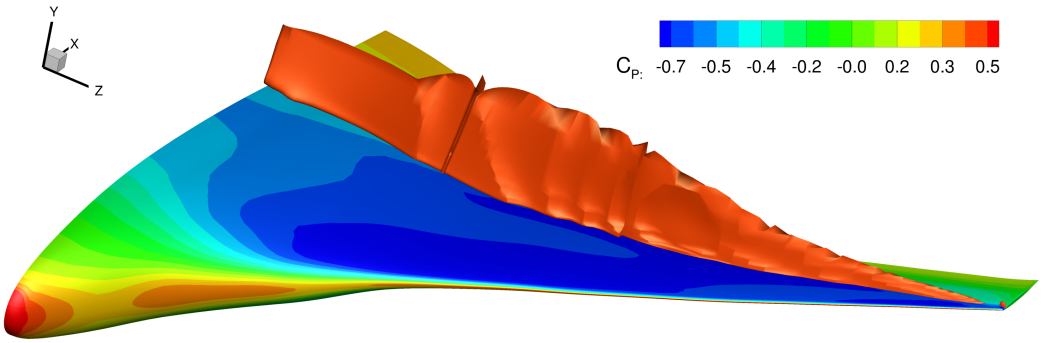

Figure 25. Shock surface on the optimized BWB at Mach 0.875

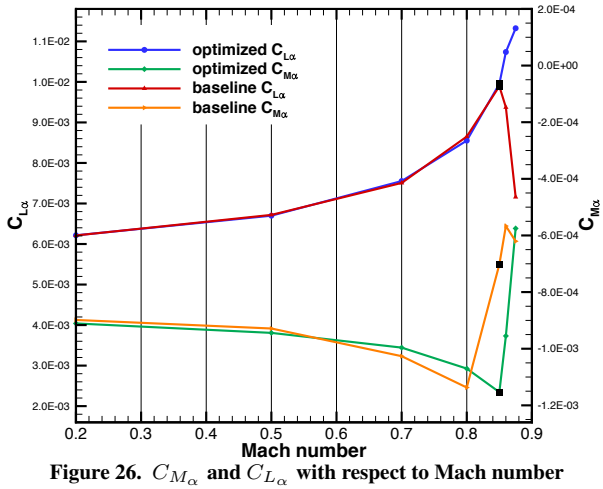

Figure 26. C_{M_α} and C_{L_α} with respect to Mach number

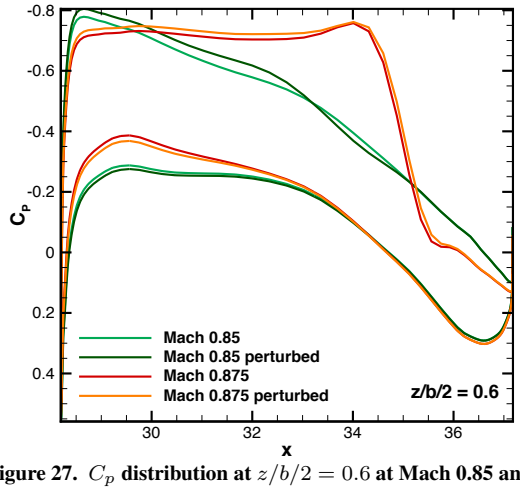

Figure 27. C_p distribution at $z/b/2 = 0.6$ at Mach 0.85 and 0.875

C. Case 3: lift-constrained drag minimization with respect to planform variables, with geometric and bending moment constraints

In this optimization case, we include planform variables in addition to the design variables and constraints in Case 2. The centerbody planform shape is kept constant. The outer wing is divided into seven sections. Each section has its own twist, chord, sweep and span design variables. The change of planform shape, especially the span variables, may increase the root bending moment, which would result in a heavier structure. We impose a center plane bending moment constraint to minimize impact on structural weight. Before the optimizing both shape and planform, we first optimize the planform and twist alone to use the result as the initial point for the full optimization. Due to the additional degrees-of-freedom, the optimization takes longer to converge. The initial planform only optimization converged in 2.5 hours, while the full optimization converged in 43 hours using 180 processors.

Figure 28 shows the pressure contour of the baseline and optimized BWB. The baseline planform shape is shown in red. The sweep angles of the outer wing decrease slightly. A raked wingtip is generated on the last two wing section. Interestingly, despite the fact that each wing section has an independent combination of sweep, twist, chord, and span,

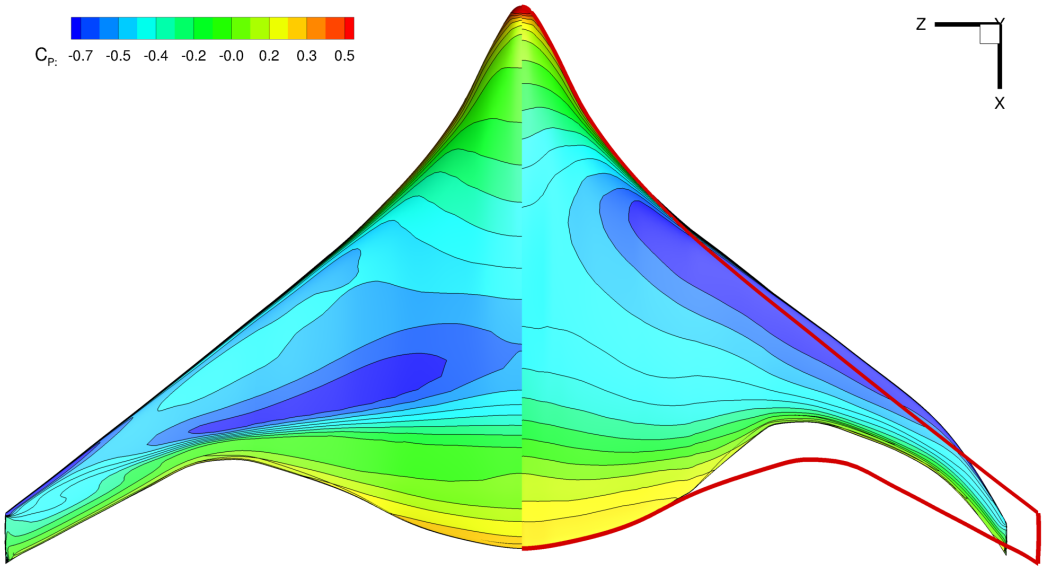

Figure 28. Pressure contour of the baseline and optimized BWB for Case 3

the optimization achieves a straight LE on the wing and on the raked tip. The kinks on the LE during the optimization are smoothed out toward the end of optimization, probably driven by the drag penalty of a kinked LE.

We can see from Figure 29 that the shock strength is reduced when compared with the baseline using only the planform variables. However, without the shape variables, the optimization is not able to completely remove the shock on the upper surface. With the addition of shape variables, the shock is completely eliminated. Aerodynamic coefficients of the baseline and optimized BWB are listed in Table 6. Unlike the previous cases, both pressure drag and skin friction drag is reduced due to the decrease in chord and span. The drag decreases by 29% with trim and root bending moment constraint satisfied. The degrees-of-freedom in planform changes allow a higher drag reduction compared to Case 2.

Coefficient	Baseline	Optimized	Difference
C_D	0.013609	0.09660	-29.0%
C_{D_P}	0.009558	0.005744	-39.9%
C_{D_V}	0.004050	0.003916	-3.3%
C_M	0.05163	0.00000	-100.0%
C_{bend}	0.1195	0.1195	0.0%

Table 6. Aerodynamic coefficients of the baseline and optimized BWB in Case 3

D. Case 4: lift-constrained drag minimization using full-turbulence adjoint

In this case, we use the full-turbulence adjoint implementation to compute gradients so that we can investigate the effects on computation cost, convergence, and optimization results. The optimization problem is the same as Case 2 in Section B. We perform lift-constrained drag minimization with respect to shape variables, with geometric, center plane bending moment, and trim constraints. Instead of using the frozen-turbulence adjoint as before, the gradients include contributions from the turbulence viscosity by linearizing the SA turbulence model that is used in the main flow solver [15]. Due to the additional state variables and a larger flux Jacobian matrix, the adjoint solution is more costly than that from the frozen-turbulence adjoint. Table 7 summarizes the computation cost for each task. The cost

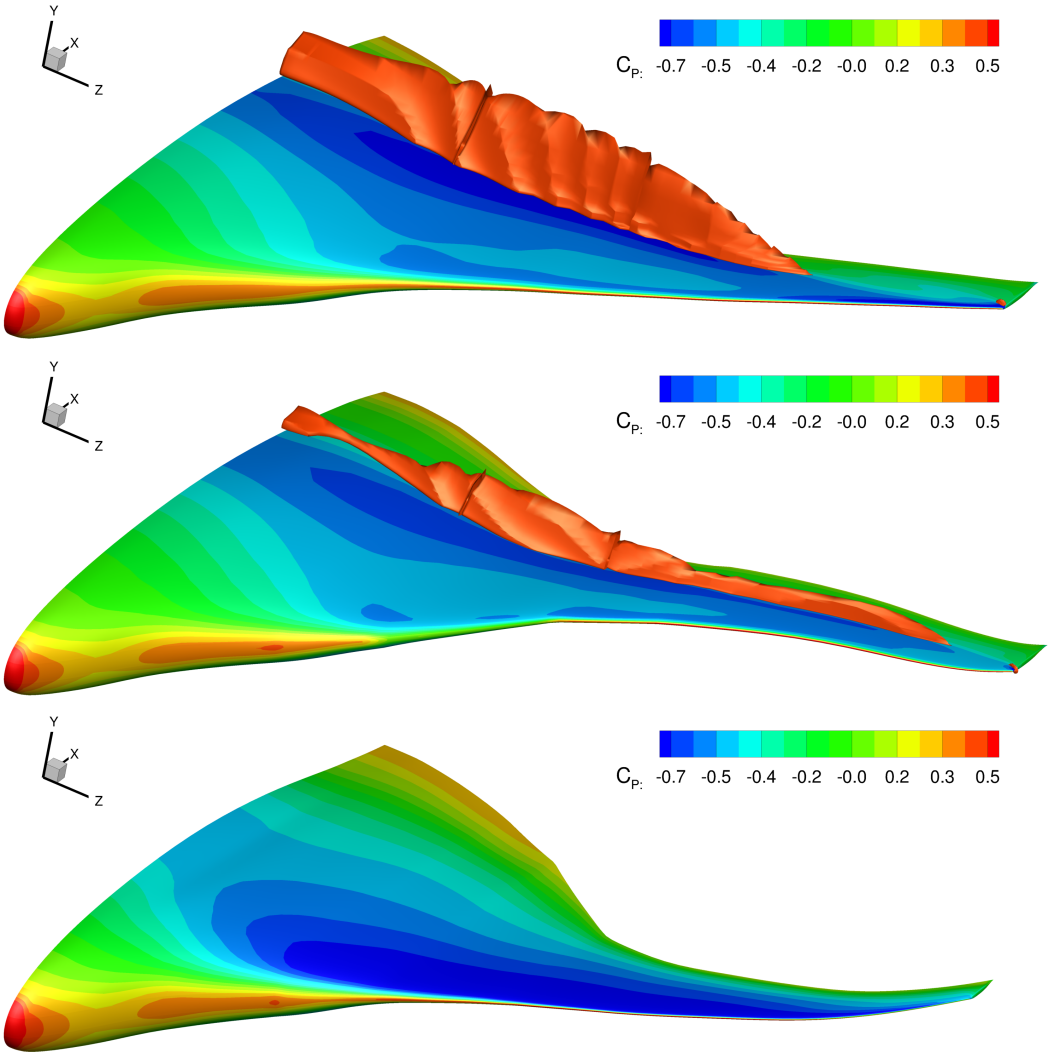

Figure 29. Shock surface on the baseline (top), initial planform optimized (middle) and the optimized (bottom) BWB

is divided into four parts: flow solution, adjoint matrix assembly, adjoint solution, and miscellaneous (I/O, geometry manipulation, total sensitivity, and optimization algorithm).

Component	Frozen-Turbulence		Full-Turbulence	
	Time (s)	Fraction (%)	Time (s)	Fraction (%)
Flow solution	393	33.8	381	27.6
Adjoint assembly	41	3.6	50	3.7
4 Adjoint solutions	686	59.0	927	67.2
Miscellaneous	42	3.6	20	1.5
Total	1162	100.0	1381	100.0

Table 7. Optimization time comparison per iteration of frozen-tubulence and full-turbulence adjoint

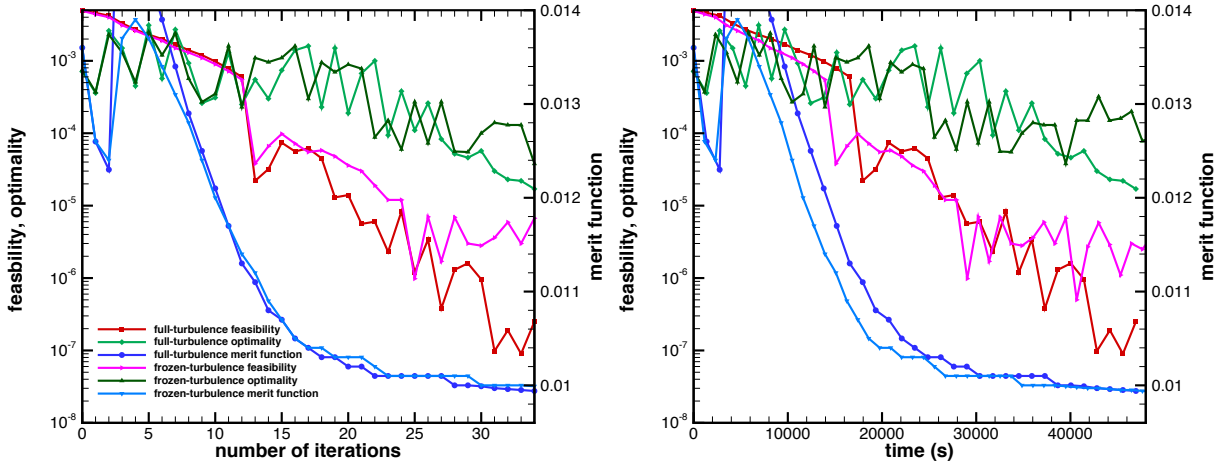

Figure 30. Feasibility, optimality and merit function comparison of the frozen-turbulence and full-turbulence adjoints with respect to the number of iterations and computational time

The full-turbulence adjoint imposes higher computation cost per iteration as well as higher memory usage.The full-turbulence adjoint does improve optimizaiton convergence to a certain extent. As shown in Figure 30, the full-turbulence merit function is always below the frozen-turbulence merit function. However, the differences are relatively small. If the computational time is considered, the frozen-turbulence adjoint still converges to a better solution for a given amount of time. We conclude that the benefit of using a full-turbulence approach cannot justify the significant increase in adjoint solution time.

V. Conclusion

The four cases for the RANS-based aerodynamic shape optimization of a BWB configuration demonstrate the benefits and impacts of various design variables and constraints. As one would expect, the optimized BWB has the lowest drag coefficient when only lift and geometric constraints are enforced. The strong shock on the upper surface is completely removed. However, this case is untrimmed and has a higher center plane bending moment than the baseline BWB. By adding both trim and bending moment constraints, the optimized drag coefficient increases by 5 counts relative to Case 1. The impact on the aerodynamic performance is mainly due to a spanwise lift distribution that is no longer close to the ideal.

We also investigated the optimized BWB in off-design conditions by performing a trimmed Mach sweep from 0.2 to 0.875. The optimized design significantly improved the drag over the entire transonic region when compared to the baseline. Low-speed drag is sacrificed to improve the high-speed performance. On the optimized design, we see a low trim drag at high speeds and high trim drag at low speeds, which differs significantly from the baseline BWB. The optimized BWB is also stable at all Mach numbers. The static margin decreases slightly from 14% to 11% at the nominal cruise condition. As Mach number increases, the shock reappears on the upper shock, which vastly reduces static margin to 5.5% at Mach 0.875.

By adding the planform variables, and additional drag reduction is achieved. The drag coefficient decreases by 29% when compared to the baseline design. Both sweep angle and chord decrease. A raked wingtip is created in the optimized design. This optimization case shows the potential of simultaneously optimizing planform and shape on new configurations, although aerostructural considerations become even more important in this case.

Finally, the effects of the frozen-turbulence assumption are assessed by performing the same optimization case with full-turbulence RANS adjoint. The higher gradient accuracy benefits the optimization, resulting in a slightly lower merit function for a fixed number of iterations. However, the full-turbulence adjoint solution takes 35% longer

than the frozen-turbulence adjoint. Thus, for a given amount of computation time, the frozen-turbulence adjoint achieves a lower merit function.

VI. Acknowledgments

The authors would like to thank Dr. Gaetan Kenway for his numerous suggestions and support to this project, including the hyperbolic mesh generator that was used in this paper. The authors would also like to thank Dr. Charles Mader for his assistance and the implementation of the nested FFD. This work is funded by Michigan/AFRL/Boeing Collaborative Center in Aeronautical Sciences (MAB-CCAS). The computations were performed on Flux HPC at the University of Michigan CAEN Advanced Computing Center, and Stampede HPC of the Extreme Science and Engineering Discovery Environment (XSEDE), which is supported by National Science Foundation grant number OCI-1053575.

References

[1] "Airlines for America Economic Reports," 2011, http://www.airlines.org/Documents/economicreports/2011.pdf.

[2] Liebeck, R. H., "Design of the Blended Wing Body Subsonic Transport," *Journal of Aircraft*, Vol. 41, No. 1, May 2004, pp. 10–25. doi:10.2514/1.9084.

[3] Kroo, I., "Innovations in Aeronautics," *42nd AIAA Aerospace Sciences Meeting*, January 2004. doi:0.2514/6.2004-1.

[4] Qin, N., Vavalle, A., Le Moigne, A., Laban, M., Hackett, K., and Weinerfelt, P., "Aerodynamic Considerations of Blended Wing Body Aircraft," *Progress in Aerospace Sciences*, Vol. 40, No. 6, 8 2004, pp. 321–343. doi:10.1016/j.paerosci.2004.08.001.

[5] Roman, D., Gilmore, R., and Wakayama, S., "Aerodynamics of High-Subsonic Blended-Wing-Body Configurations," *41st Aerospace Sciences Meeting and Exhibit*, 2003. doi:10.2514/6.2003-554.

[6] Liebeck, R., "Design of the Blended-Wing-Body Subsonic Transport," *40th AIAA Aerospace Sciences Meeting & Exhibit*, 2002. doi:10.2514/6.2002-2.

[7] Wakayama, S., "Multidisciplinary Design Optimization of the Blended-Wing-Body," *7TH AIAA Symposium on Multidisciplinary Analysis And Optimization*, 1998. doi:10.2514/6.1998-4938.

[8] Wakayama, S., "Blended-Wing-Body Optimization Problem Setup," *8th Symposium on Multidisciplinary Analysis and Optimization*, 2000. doi:10.2514/6.2000-4740.

[9] Qin, N., Vavalle, A., and Moigne, A. L., "Spanwise Lift Distribution for Blended Wing Body Aircraft," *Journal of Aircraft*, Vol. 42, No. 2, 2005, pp. 356–365. doi:10.2514/1.4229.

[10] Peigin, S. and Epstein, B., "Computational Fluid Dynamics Driven Optimization Of Blended Wing Body Aircraft," *AIAA Journal*, Vol. 44, No. 11, 2006, pp. 2736–2745. doi:10.2514/1.19757.

[11] Kuntawala, N. B., *Aerodynamic Shape Optimization of a Blended-Wing-Body Aircraft Configuration*, Master's thesis, University of Toronto, 2011.

[12] Kuntawala, N. B., Hicken, J. E., and Zingg, D. W., "Preliminary Aerodynamic Shape Optimization Of A Blended-Wing-Body Aircraft Configuration," *49th AIAA Aerospace Sciences Meeting, Orlando, Florida*, 2011. doi:10.2514/6.2011-642.

[13] Meheut, M., Arntz, A., and Carrier, G., "Aerodynamic Shape Optimizations of a Blended Wing Body Configuration for Several Wing Planforms," *30th AIAA Applied Aerodynamics Conference*, 2012. doi:10.2514/6.2012-3122.

[14] Lyu, Z. and Martins, J. R. R. A., "Aerodynamic Shape Optimization of a Blended-Wing-Body Aircraft," *51st AIAA Aerospace Sciences Meeting including the New Horizons Forum and Aerospace Exposition*, 2013. doi:10.2514/6.2013-283.

[15] Lyu, Z., Kenway, G., Paige, C., and Martins, J. R. R. A., "Automatic Differentiation Adjoint of the Reynolds-Averaged Navier-Stokes Equations with a Turbulence Model," *43rd AIAA Fluid Dynamics Conference and Exhibit*, June 2013.

[16] Kenway, G. K. W., Kennedy, G. J., and Martins, J. R. R. A., "A Scalable Parallel Approach for High-Fidelity Steady-State Aeroelastic Analysis and Adjoint Derivative Computations," *AIAA Journal*, 2013.

[17] Kenway, G. K. W. and Martins, J. R. R. A., "Multi-point High-fidelity Aerostructural Optimization of a Transport Aircraft Configuration," *Journal of Aircraft*, 2013.

[18] Kenway, G. K., Kennedy, G. J., and Martins, J. R. R. A., "A CAD-free Approach to High-Fidelity Aerostructural Optimization," *Proceedings of the 13th AIAA/ISSMO Multidisciplinary Analysis Optimization Conference, Fort Worth, TX*, 2010. doi:10.2514/6.2010-9231.

[19] Kota, S., Osborn, R., Ervin, G., Maric, D., Flick, P., and Paul, D., "Mission Adaptive Compliant Wing–Design, Fabrication and Flight Test," *RTO Applied Vehicle Technology Panel (AVT) Symposium*, 2009.

[20] van der Weide, E., Kalitzin, G., Schluter, J., and Alonso, J., "Unsteady Turbomachinery Computations Using Massively Parallel Platforms," *44th AIAA Aerospace Sciences Meeting and Exhibit*, 2006. doi:10.2514/6.2006-421.

[21] Jameson, A., Schmidt, W., and Turkel, E., "Numerical Solution of the Euler equations by Finite Volume Methods Using Runge Kutta Time Stepping Schemes," *14th AIAA, Fluid and Plasma Dynamics Conference*, 1981.

[22] Mader, C. A., Martins, J. R. R. A., Alonso, J. J., and van der Weide, E., "ADjoint: An Approach for the Rapid Development of Discrete Adjoint Solvers," *AIAA Journal*, Vol. 46, No. 4, April 2008, pp. 863–873. doi:10.2514/1.29123.

[23] Saad, Y. and Schultz, M. H., "GMRES: A Generalized Minimal Residual Algorithm for Solving Nonsymmetric Linear Systems," *SIAM Journal on Scientific and Statistical Computing*, Vol. 7, No. 3, 1986, pp. 856–869. doi:10.1137/0907058.

[24] Balay, S., Gropp, W. D., McInnes, L. C., and Smith, B. F., "Efficient Management of Parallelism in Object Oriented Numerical Software Libraries," *Modern Software Tools in Scientific Computing*, edited by E. Arge, A. M. Bruaset, and H. P. Langtangen, Birkhäuser Press, 1997, pp. 163–202. doi:10.1007/978-1-4612-1986-6_8.

[25] Balay, S., Brown, J., , Buschelman, K., Eijkhout, V., Gropp, W. D., Kaushik, D., Knepley, M. G., McInnes, L. C., Smith, B. F., and Zhang, H., "PETSc Users Manual," Tech. Rep. ANL-95/11 - Revision 3.4, Argonne National Laboratory, 2013.

[26] Balay, S., Brown, J., Buschelman, K., Gropp, W. D., Kaushik, D., Knepley, M. G., McInnes, L. C., Smith, B. F., and Zhang, H., "PETSc Web page," 2013, http://www.mcs.anl.gov/petsc.

[27] Perez, R. E., Jansen, P. W., and Martins, J. R. R. A., "pyOpt: A Python-Based Object-Oriented Framework for Nonlinear Constrained Optimization," *Structures and Multidisciplinary Optimization*, Vol. 45, No. 1, 2012, pp. 101–118. doi:10.1007/s00158-011-0666-3.

[28] Gill, P. E., Murray, W., and Saunders, M. A., "SNOPT: An SQP algorithm for large-scale constrained optimization," *SIAM journal on optimization*, Vol. 12, No. 4, 2002, pp. 979–1006. doi:10.1137/S1052623499350013.

[29] Mader, C. A. and Martins, J. R. R. A., "Optimal Flying Wings: A Numerical Optimization Study," *53rd AIAA/ASME/ASCE/AHS/ASC Structures, Structural Dynamics, and Materials Conference*, Honolulu, HI, April 2012. doi:10.2514/6.2012-1758, AIAA 2012-1758.